RSC Advances

RSC Publishing

PAPER

View Article Online
View Journal | View Issue

Cite this: *RSC Advances*, 2013, **3**, 12409

The role of iron oxide in the highly effective Fe-modified Co_3O_4 catalyst for low-temperature CO oxidation

Jie Li,[a] Guanzhong Lu,*[ab] Guisheng Wu,[b] Dongsen Mao,[b] Yanglong Guo,[a] Yanqin Wang[a] and Yun Guo[a]

Received 21st March 2013,
Accepted 10th May 2013

DOI: 10.1039/c3ra41272e

www.rsc.org/advances

A series of iron modified cobalt oxide catalysts ($Fe_aCo_bO_x$ ($b : a = M_{Co} : M_{Fe}$, $10 < x < 15$)) were prepared by a co-precipitation method, characterized by nitrogen adsorption–desorption, XRD, Raman spectroscopy, XPS, H_2-temperature programmed reduction, CO-temperature-programmed desorption, O_2-temperature-programmed desorption and time-resolved CO titration, and their catalytic activities for CO oxidation were evaluated. When Co : Fe is 8 : 2 (mol), the $Fe_2Co_8O_x$ catalyst exhibits a very high catalytic activity, in which CO can be completely converted to CO_2 at −80 °C. The results show that the addition of Fe to Co_3O_4 can increase its surface area and inhibit the agglomeration of iron oxide, improve the reduction behaviour of Co_3O_4, optimize the ratio of Co^{3+} : Co^{2+} on the catalyst surface, and promote CO adsorption and CO_2 desorption on the catalyst surface. The oxygen species on $Fe_2Co_8O_x$ are more active than those on Co_3O_4, and when the feed gas is lacking in oxygen the lattice oxygen of $Fe_2Co_8O_x$ can easily overflow to the surface to participate in the oxidation of CO.

1. Introduction

Catalytic oxidation of CO is one of many very important reactions in the catalysis field owing to its applications in indoor air cleaning, automotive exhaust treatment, CO_2 lasers, breathing apparatus and fuel cells *etc*. Researchers with a tremendous interest have paid close attention to low-temperature CO oxidation, due to the demand for low-temperature automobile exhaust catalysts. A large amount of emissions from cars are released during the first minutes after a cold start, before the catalyst becomes hot enough to convert the harmful emissions.[1,2] Also, new and fuel-efficient engines generate colder exhaust gases than the current engines, resulting in the slower heating of the three-way catalysts. This places a great demand on low-temperature activity for the catalytic converters used in future emission abatement systems. Low-temperature CO oxidation also plays a crucial role in the control of exhaust gases in highway tunnels and underground parking garages *etc.*, as vehicles enter these places often in an idle and slow speed state, which will cause incomplete combustion of gasoline, leading to high concentrations of exhaust gases (such as CO and hydrocarbon (HC_x) compounds).

For low-temperature CO oxidation, precious metal (PM) catalysts exhibit a high activity, and are widely used for the exhaust gas emission control.[3–5] However, the high cost of the PMs and the ease of which the PM catalysts are poisoned by sulphur, limits their commercial applications and forces researchers to find alternative transition metal oxide catalysts which can be used instead of the PM catalysts.[6–12] Among the transition metal oxide catalysts, cobalt oxide has attracted considerable attention due to its high catalytic activity for CO oxidation.[9–14] However, the stability of cobalt oxide is poor and it can be severely deactivated by trace amounts of moisture included in the feed gas. Also, the high performance of the cobalt oxide catalysts depends greatly on the preparation methods, for instance, Xie *et al.*[13] applied morphology control methods to prepare Co_3O_4 with a high activity and stability. It is known that the catalytic activity of cobalt oxide can be modified by controlling its particle size, or doping with foreign oxides.[15,16] In this paper, we adopted the modification method with a foreign element (iron) to improve the catalytic performance of cobalt oxide.

Iron oxide has been widely used as the catalyst component in many industrial processes, such as dehydrogenation, oxidation, and the Fischer–Tropsch synthesis *etc*.[17–19] Also, iron oxide is often used as the support for precious metal catalysts for low-temperature CO oxidation. Haruta *et al.*[20] developed an Au catalyst which was supported on a Fe_2O_3 support for CO oxidation at room temperature. Liu *et al.*[21] found that in Pt and Pd catalysts supported on FeO_x, FeO_x can

[a]*Key Laboratory for Advanced Materials and Research Institute of Industrial catalysis, East China University of Science and Technology, Shanghai 200237, P. R. China. E-mail: gzhlu@ecust.edu.cn; Fax: +86-21-64253824*
[b]*Research Institute of Applied Catalysis, Shanghai Institute of Technology, Shanghai 200235, P. R. China*

supply active oxygen to react with CO. Natile and Glisenti[22] studied the oxidation of methanol on NiO–Co_3O_4 and Fe_2O_3–Co_3O_4 catalysts, and found that methanol can dissociate from Fe_2O_3–Co_3O_4 through the formation of a formic species, even at room temperature. There was only a very weak reaction of methanol with the catalyst surface when NiO–Co_3O_4 was used as the catalyst. Until now, studies about the FeO_x catalyst have mainly been focused on the FeO_x supported precious metal catalysts and the Fischer–Tropsch synthesis reaction *etc*. The FeO_x promoted cobalt oxide catalyst for CO oxidation has been rarely reported.

Herein, we have developed a highly effective Fe-modified Co_3O_4 catalyst for low-temperature CO oxidation, and investigated the effect of iron on the physicochemical and catalytic properties of the Co_3O_4 catalyst. The $Fe_2Co_8O_x$ catalyst prepared by a co-precipitation method exhibits a very high catalytic activity for CO oxidation and its complete conversion temperature reaches −80 °C.

2. Experimental section

2.1 Catalyst preparation

The $Fe_aCo_bO_x$ mixed oxide catalysts were prepared by a co-precipitation method. Weighed $Fe(NO_3)_3{\cdot}9H_2O$ and $Co(NO_3)_2{\cdot}6H_2O$ were dissolved in de-ionized water at room temperature, and then the sodium carbonate solution (1 M) was added to this solution with continuous stirring until pH 9 was reached. After being kept under these conditions for 2 h, the formed precipitates were filtered, washed with de-ionized water several times, then dried in air at 110 °C overnight and calcined for 3 h at 350 °C in a muffle furnace. Pure Co_3O_4 and FeO_x were prepared by the same procedures as the $Fe_aCo_bO_x$ mixed oxide catalysts.

2.2 Characterization of the catalysts

The BET surface areas of the samples were measured by N_2 adsorption–desorption at −196 °C on a micromeritics ASAP-2020 instrument and calculated by the Brunauer–Emmett–Teller (BET) method. Elemental analysis for the samples was obtained using inductively coupled-plasma atomic emission spectroscopy (ICP-AES) on a TJA IRIS ADVANTAG 1000 instrument. Powder X-ray diffraction (XRD) patterns were recorded on a PANalytical PW 3040/60 X'Pert Pro powder diffractometer using Cu-Kα radiation, which was operated at 40 kV and 40 mA with a scanning speed of 0.5° min^{-1}. Transmission electron microscopy (TEM) images were obtained using a JEOL JEM-2100 microscope operating at 200 kV, and the sample to be measured was first dispersed in ethanol and then collected on a copper grid covered with a carbon film. After the liquid phase was evaporated the grid was loaded into the microscope. X-ray photoelectron spectroscopy (XPS) spectra of the samples were obtained using a Kratos Axis Ultra-DLD photoelectron spectrometer equipped with a monochromatic Al-Kα (1486.6 eV) X-ray source. Before the experiment, the sample was pretreated with N_2 at 500 °C for 30 min. All binding energies (BE) were determined with respect to the C1s line (284.8 eV) originating from adventitious carbon. Laser Raman spectra of the samples were obtained using a Renishaw Raman spectrometer under ambient conditions and the 514 nm line of a Spectra Physics Ar^+ laser was used as an excitation source. The laser beam intensity and the spectrum slit width were 2 mW and 3.5 cm^{-1}, respectively.

The H_2-temperature programmed reduction (H_2-TPR) was performed in a quartz U-tube with 50 mg catalyst (40–60 mesh). After the catalyst was pretreated in N_2 at 500 °C for 30 min, it was cooled down to room temperature and then a mixture of 10 vol% H_2–N_2 (25 ml min^{-1}) was used instead of N_2. The heating rate was 10 °C min^{-1}. The uptake amounts of H_2 were measured by a thermal conductivity detector (TCD).

The temperature-programmed desorption of O_2 (O_2-TPD) and CO (CO-TPD) adsorbed on the sample was performed in a quartz tube reactor system equipped with a quadrupole mass spectrometer (MS, IPC 400, INFICON Co. Ltd.). A 200 mg sample (40–60 mesh) was pretreated in N_2 at 500 °C for 30 min. After it was cooled down to room temperature, pure O_2 (30 ml min^{-1}) or pure CO (30 ml min^{-1}) was introduced through the catalyst bed for 60 min. He (30 ml min^{-1}) was then introduced instead of pure O_2 or pure CO, and the temperature was raised to 750 °C at a heating rate of 10 °C min^{-1}. The mass signals of O_2 (m/z = 32), CO (m/z = 28) and CO_2 (m/z = 44) were recorded.

The time-resolved CO titrations were carried out as follows: a 200 mg sample was pretreated in pure He (30 ml min^{-1}) at 600 °C for 30 min, and then cooled to room temperature in He. Subsequently, 5% CO–He (30 ml min^{-1}) was introduced, and both the CO and CO_2 signals were recorded by a quadrupole MS detector.

2.3 Catalytic activity testing

The catalytic activities of the catalysts for CO oxidation were tested in a continuous flow quartz tube microreactor (Ø 8 mm × 23 cm). 200 mg catalyst (40–60 mesh) and 600 mg silica sand were mixed and added to the reactor. The flow rate of the feed gases, consisting of 1% CO, 10% O_2 and 89% N_2, was 20 ml min^{-1}. Before activity testing, the catalysts were pretreated in a N_2 flow at 500 °C for 30 min and then cooled down to room temperature.

3. Results and discussion

3.1 Catalytic activity

The catalytic conversion of CO as a function of temperature over the Co_3O_4 and $Fe_aCo_bO_x$ catalysts is shown in Fig. 1. The results show that Co_3O_4 has a pretty good activity for CO oxidation with a CO complete conversion temperature (T_{100}) of −49 °C and after adding iron to Co_3O_4, the $Fe_aCo_bO_x$ catalyst exhibited a much higher catalytic activity than the single Co_3O_4 catalyst. Among the $Fe_aCo_bO_x$ catalysts, $Fe_2Co_8O_x$ shows the highest catalytic activity, for instance, at −80 °C, CO can be completely converted to CO_2. The T_{100} values of all the catalysts are listed in Table 1.

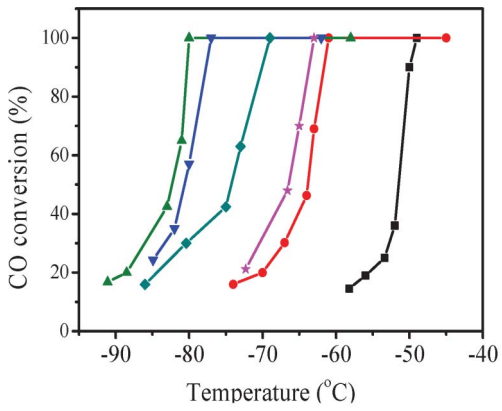

Fig. 1 The catalytic activities of the Co_3O_4 and $Fe_aCo_bO_x$ catalysts for CO oxidation. (■) Co_3O_4; (●) $Fe_1Co_9O_x$; (▲) $Fe_2Co_8O_x$; (▼) $Fe_3Co_7O_x$; (◆) $Fe_4Co_6O_x$; (★) $Fe_6Co_4O_x$.

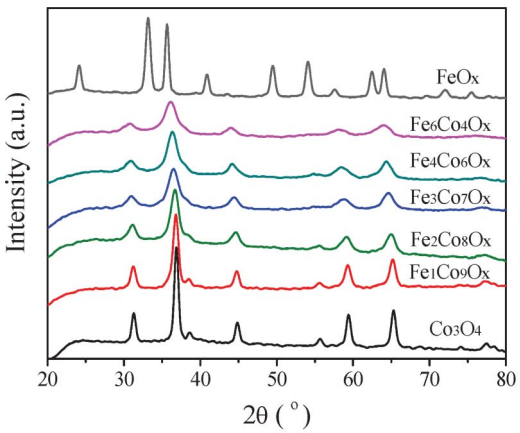

Fig. 2 XRD patterns of the Co_3O_4, FeO_x and $Fe_aCo_bO_x$ catalysts.

3.2 N_2 adsorption–desorption and XRD

The BET surface areas (S_{BET}) of the samples obtained from the N_2 adsorption–desorption experiments are shown in Table 1. The results show that the surface areas (110–130 $m^2\ g^{-1}$) of the $Fe_aCo_bO_x$ ($b : a \leqslant 8 : 2$) catalysts are much higher than those ($\sim$60 $m^2\ g^{-1}$) of the single Co_3O_4 and Fe_2O_3 samples, and when $b : a > 8 : 2$ ($Fe_1Co_9O_x$), its surface area is only 79.6 $m^2\ g^{-1}$. The compositions of the $Fe_aCo_bO_x$ samples were detected by ICP-AES and the $M_{Co} : M_{Fe}$ molar ratios are listed in Table 1.

The XRD patterns of the $Fe_aCo_bO_x$ catalysts are shown in Fig. 2. The results show that the FeO_x sample exhibits the perfect diffraction peaks of the rhombohedral crystalline phase of α-Fe_2O_3 (JCPDS card 81-2810), and the cobalt oxide sample exhibits the characteristic diffraction peaks of the cubic spinel structure Co_3O_4 (JCPDS card 43-1003). After Fe was added to Co_3O_4, the diffraction peaks of the $Fe_aCo_bO_x$ catalysts were the same as those seen for the spinel structure of Co_3O_4 and the diffraction peaks for α-Fe_2O_3 were not observed. The higher the Fe loading in the $Fe_aCo_bO_x$ sample, the broader the Co_3O_4 diffraction peaks became. This may be attributed to the diminishment of the crystal size, because the diffraction peaks gradually would shift to a lower angle with an increase in the Fe loading. The results in Table 1 show that increasing the Fe loading leads to an increase in the cell parameter (a) of Co_3O_4. This is due to the fact that the atom radius of Fe is a little bigger than that of Co, and after the Fe ions penetrate into the crystal of Co_3O_4 to form a solid solution, the crystal cells expand.

Table 1 The BET surface areas (S_{BET}), cell parameters (a), T_{100} values and molar ratios of $M_{Co} : M_{Fe}$ for the $Fe_aCo_bO_x$ catalysts

Sample	S_{BET} ($m^2\ g^{-1}$)	a (nm)	T_{100} (°C)	$M_{Co} : M_{Fe}$ In solution	$M_{Co} : M_{Fe}$ In solid
Co_3O_4	59.8	0.8077	−49		
$Fe_1Co_9O_x$	79.6	0.8098	−61	9.00	8.81
$Fe_2Co_8O_x$	109	0.8099	−80	4.00	4.77
$Fe_3Co_7O_x$	126	0.8162	−78	2.33	2.24
$Fe_4Co_6O_x$	108	0.8179	−69	1.50	1.52
$Fe_6Co_4O_x$	129	0.8216	−63	0.67	0.62
FeO_x	59.5				

3.3 Transmission electron microscopy (TEM)

Transmission electron microscopy (TEM) was employed to observe the morphologies of the catalysts, and the TEM images of Co_3O_4, $Fe_2Co_8O_x$ and $Fe_6Co_4O_x$ are shown in Fig. 3. The results show that the three samples are of good crystallinity. Co_3O_4 and $Fe_2Co_8O_x$ exhibit a similar morphology (approximately a hexagonal pattern), with a crystallite size of

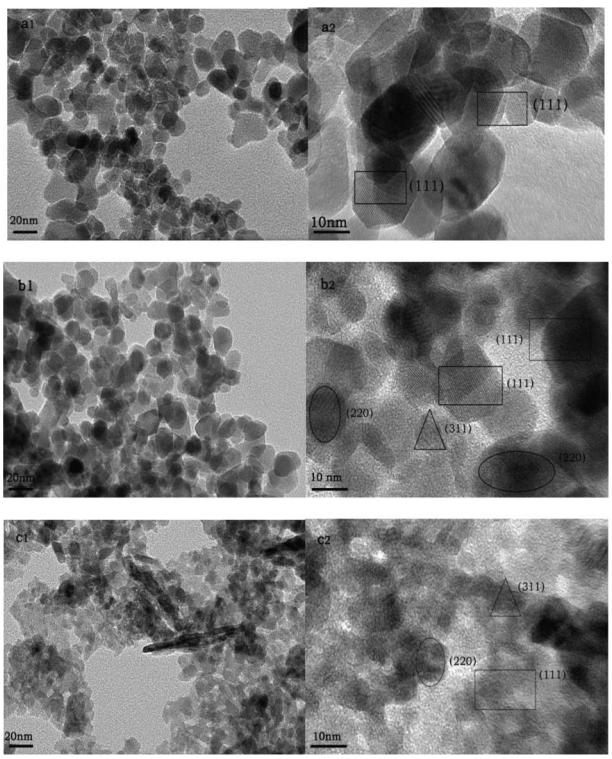

Fig. 3 TEM images of Co_3O_4 (a_1, a_2), $Fe_2Co_8O_x$ (b_1, b_2) and $Fe_6Co_4O_x$ (c_1, c_2).

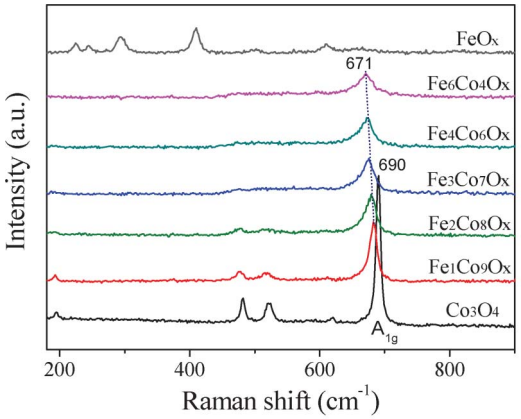

Fig. 4 Laser Raman spectra of the Co_3O_4, FeO_x and $Fe_aCo_bO_x$ catalysts using a 514.5 nm excitation source.

10–20 nm, which is typical of the spinel structure. In contrast to the Co_3O_4 and $Fe_2Co_8O_x$ samples, the $Fe_6Co_4O_x$ crystallites agglomerated to form thin sheet and rodlike species with unclear edges, which shows that adding an amount of iron to the sample makes the catalyst particles accrete by agglomeration and growth. In the TEM image of Co_3O_4 (Fig. 3a$_2$) we can see that there are (111) planes with spacings of 0.462 nm, which are typical of the face-centered cubic structure. For the $Fe_2Co_8O_x$ (Fig. 3b$_2$) and $Fe_6Co_4O_x$ (Fig. 3c$_2$) samples, (111) planes (0.462 nm), (220) planes (0.282 nm) and (311) planes (0.243 nm) can be clearly observed, which are different planes of the spinel structure.

3.4 Laser Raman spectroscopy

The Raman spectra of the Co_3O_4, FeO_x and $Fe_aCo_bO_x$ catalysts are shown in Fig. 4. Raman bands at 193, 482, 522, 620 and 690 cm^{-1} can be observed for the crystalline Co_3O_4.[23–25] The band at 690 cm^{-1} is attributed to the A_{1g} symmetry of the octahedral sites (CoO_6) in the *O* spectroscopic group,[26] and the bands at 482 and 522 cm^{-1} are attributed to the E_g and *F* symmetry, respectively. The weak band at 620 cm^{-1} possesses *F* symmetry. The band at 193 cm^{-1} is attributed to the characteristics of the tetrahedral sites (CoO_4) with *F* symmetry.[26] The vibration mode of FeO_x may be attributed to Fe_2O_3.[27] The Raman spectra of the $Fe_aCo_bO_x$ catalysts are similar to that of Co_3O_4, in which the vibration bands of Fe_2O_3 cannot be observed, even for the sample with $M_{Co} : M_{Fe} = 4 : 6$. This result proves the results from the XRD in Fig. 2, that is, iron does not exist in the form of Fe_2O_3 but becomes integrated in the spinel structure of the cobalt oxide. When increasing the Fe loading in the $Fe_aCo_bO_x$ catalyst, its vibration band of A_{1g} shifts to a low wavenumber, which is a sensitive indication of the highly defective structure.[28] Therefore, the iron containing Co_3O_4 sample possesses more surface defects, resulting in an improvement of its catalytic activity.[29]

3.5 X-ray photoelectron spectroscopy

As we all know, in the XPS spectra of Co(II) high-spin compounds, such as CoO, there are intense shake-up satellite peaks at ~787.0 and 804.0 eV. Unlike the Co(II) compounds, in

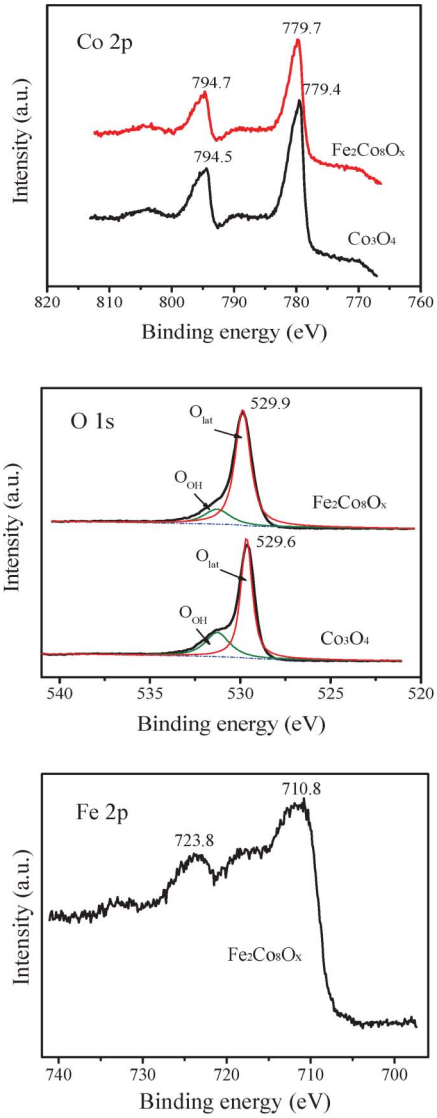

Fig. 5 The Co 2p, O 1s and Fe 2p XPS spectra of Co_3O_4 and $Fe_2Co_8O_x$.

the XPS spectra of low-spin Co(III) compounds, the satellite peaks are weak or missing.[30] Co_3O_4 is a mixed-valence oxide, and its Co 2p XPS spectrum is symptomatic of the weak shake-up satellite structure due to the minor Co(II) component.[31] The Co 2p XPS spectra of Co_3O_4 and $Fe_2Co_8O_x$ in Fig. 5 show that the satellite structure of $Fe_2Co_8O_x$ is weaker than that of Co_3O_4, which may be due to the higher ratio of $Co^{3+} : Co^{2+}$ in $Fe_2Co_8O_x$ than in Co_3O_4. The binding energy of the Co $2p_{3/2}$ peak for Co_3O_4 is ~779.4 eV, which is the same as that previously reported.[32] The binding energy of Co $2p_{3/2}$ increased after the addition of Fe into Co_3O_4, which suggests an increase in the ratio of $Co^{3+} : Co^{2+}$ in the $Fe_2Co_8O_x$ catalyst. In the cobalt oxide-based catalysts for the CO oxidation, such as the CoO_x–CeO_2 catalyst[33] and the MnO_x modified Co_3O_4–CeO_2 catalyst,[34] the Co^{3+} ions are thought to be the active sites. Therefore, an increase in the ratio of $Co^{3+} : Co^{2+}$ caused by the introduction of Fe may be an essential factor for improving the catalytic activity of the $Fe_2Co_8O_x$ catalyst.

The O 1s XPS spectra in Fig. 5 consist of two peaks attributing to two kinds of oxygen species. The peak at a lower binding energy (~529.6 eV) is associated with lattice oxygen, and the peak at ~531.3 eV may be usually assigned to the presence of hydroxyl groups or other oxygen-containing groups.[35] Compared with the Co_3O_4 catalyst, the O 1s peak of $Fe_2Co_8O_x$ shifts slightly toward a higher binding energy, which indicates that the electronic density of oxygen is decreased and more oxygen vacancies have formed on the surface of $Fe_2Co_8O_x$ after adding Fe to Co_3O_4. For the peak at 531.3 eV, the one due to $Fe_2Co_8O_x$ is weaker than the one due to Co_3O_4 without Fe. The results in Fig. 5 show that the ratio of $O_{Lattice}$: O_{OH} for Co_3O_4 is 2.32, and 4.61 for $Fe_2Co_8O_x$, that is to say, the amount of hydroxyl groups on $Fe_2Co_8O_x$ is less than the amount on Co_3O_4 after the N_2 pretreatment at a high temperature (at 500 °C for 30 min), which shows that the surface hydroxyl groups on $Fe_2Co_8O_x$ can be removed and more oxygen vacancies can be formed.

The Fe 2p XPS spectrum of $Fe_2Co_8O_x$ (Fig. 5) displays the main peaks of Fe $2p_{3/2}$ (710.8 eV) and Fe $2p_{1/2}$ (723.8 eV) together with a weak satellite structure between the spin–orbit doublet, which corresponds to the Fe^{3+} surface species.[36] This result shows that iron exists in the +3 state in the $Fe_2Co_8O_x$ sample.

3.6 H_2-TPR

The TPR profiles in Fig. 6 show that the Co_3O_4 catalyst exhibits two reduction peaks. In general, the low-temperature peak (α) is assigned to the reduction of Co^{3+} to Co^{2+} and the high temperature peak (β) to the reduction of Co^{2+} to Co^0.[37–40] The doping of iron makes the α peak shift a little to a higher temperature and has a significant influence on the β peak. With an increase in the Fe amount, the β peak merges gradually with the reduction peak of iron, which is in agreement with previous reports.[41–43] Comparing with the reduction peak of pure Fe_2O_3, the merged peak shifts to a lower temperature, that is to say, the reduction of iron became easier due to the formation of the Fe–Co oxide solid solution.

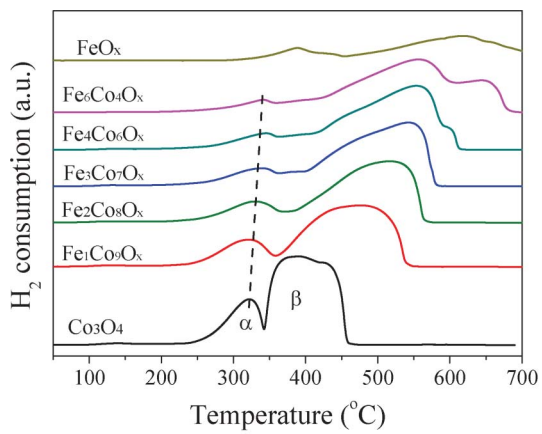

Fig. 6 H_2-TPR profiles of the Co_3O_4, FeO_x and $Fe_aCo_bO_x$ samples.

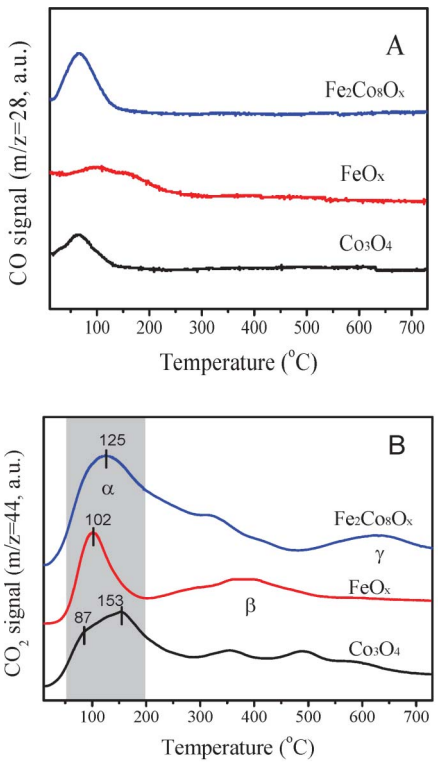

Fig. 7 Desorption profiles for CO (A) and CO_2 (B) during the TPD of CO adsorbed on the samples.

3.7 CO-TPD and O_2-TPD

In the TPD process of CO adsorbed on the catalyst with 30 ml min^{-1} He, the CO (m/z = 28) and CO_2 (m/z = 44) curves obtained are shown in Fig. 7. The results show that the desorption peak of CO on Fe_2O_3 is different from those on $Fe_2Co_8O_x$ and Co_3O_4. The CO desorption peak on Fe_2O_3 is very small and its desorption temperature is higher than on $Fe_2Co_8O_x$ and Co_3O_4, which shows that the chemically adsorbed bond of CO on Fe_2O_3 is stronger than on $Fe_2Co_8O_x$ or Co_3O_4. The presence of Fe in Co_3O_4 does not affect the adsorption property of Co_3O_4 for CO, but increases some desorption peak area of CO on Co_3O_4.

In the curves (Fig. 7B) for the CO_2 desorption on the three samples, there are three kinds (α, β, γ) of CO_2 desorption peaks, which result from the reaction of adsorbed CO with the surface oxygen. As the middle temperature peak (β) and high temperature peak (γ) are hardly related with the low-temperature catalytic activity of the catalyst for CO oxidation, here the low-temperature peak (α) is discussed only. For the α peak of CO_2 desorption on $Fe_2Co_8O_x$, its peak temperature (T_p) is 102 °C, and the T_p values on Co_3O_4 are 87 °C and 153 °C. The area of the α peak is obviously increased after adding iron to Co_3O_4 and its T_p shifts to 125 °C. These results indicate that the presence of Fe in $Fe_2Co_8O_x$ promotes the CO adsorption on the catalyst and the reaction between the adsorbed CO and the surface oxygen.

Fig. 8 shows the O_2-TPD profiles of the samples. There are four kinds of desorption peaks at ~40 °C, 185 °C, 325 °C and

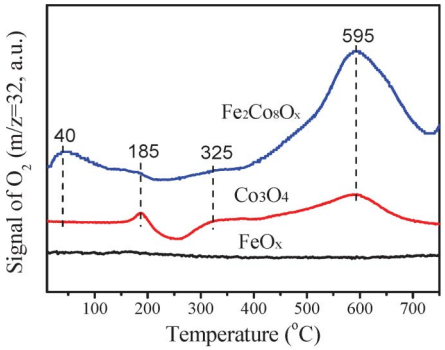

Fig. 8 O_2-TPD profiles of the samples.

595 °C, which may be assigned to O_2 (ad), O_2^- (ad), O^- (ad) and O^{2-} (lattice), respectively.[44,45] In general, the physically adsorbed oxygen O_2 (ad) is the easiest to desorb and the lattice oxygen O^{2-} (lattice) is the most difficult to desorb. The results show that the oxygen species desorbed on Fe_2O_3 are hardly found in the O_2-TPD curve, and for the Co_3O_4 sample, there are three small desorption peaks of oxygen at 185 °C, 325 °C and 595 °C respectively. After adding iron to Co_3O_4, the O_2-TPD curve changes obviously, for instance, in the O_2-TPD curve of $Fe_2Co_8O_x$, a new desorption peak at 40 °C can be observed and the desorption at 595 °C is much larger than that of the Co_3O_4 sample. These results indicate that the presence of Fe in the $Fe_2Co_8O_x$ catalyst increases remarkably the mobility and activity of the lattice oxygen in Co_3O_4 and the physical adsorption of oxygen on the surface of Co_3O_4, that is, the oxygen species on the $Fe_2Co_8O_x$ catalyst, is more active than on the Co_3O_4 catalyst, which is very important for the catalyst when used in the CO oxidation.

3.8 Time-resolved CO titration

The time-resolved CO titration technique was used to investigate the activity and reactivity of the oxygen species over the catalyst. The results of the O_2-TPD experiments show that plenty of lattice oxygen on the $Fe_2Co_8O_x$ catalyst can desorb at ~600 °C (Fig. 9). Thus, in this testing the catalysts were pretreated in a He flow at 600 °C for 30 min to remove the surface oxygen. Then 5% CO–He was flowed through the reactor, the CO and CO_2 signals were recorded by mass spectrometry, and the results for the Co_3O_4 and $Fe_2Co_8O_x$ catalysts are shown in Fig. 9.

As can be seen from Fig. 9A, there is a small CO_2 desorption peak on the Co_3O_4 catalyst after CO was introduced, and for the $Fe_2Co_8O_x$ catalyst, a large desorption peak of CO_2 can be observed (Fig. 9B), which indicates that $Fe_2Co_8O_x$ is more available to convert CO to CO_2 by bulk lattice oxygen. Furthermore, the CO_2 desorption peak on $Fe_2Co_8O_x$ is much broader than that on Co_3O_4, illustrating that the bulk lattice oxygen of $Fe_2Co_8O_x$ can overflow to the surface to participate in the oxidation of CO for a relatively longer time, because the lattice oxygen causes a slow and broad CO_2 response.[46] In comparison with the CO desorption curve on Co_3O_4, there is a sharp decrease at ~12 min in the CO desorption curve on $Fe_2Co_8O_x$, which is attributed to adsorbed CO reacting with

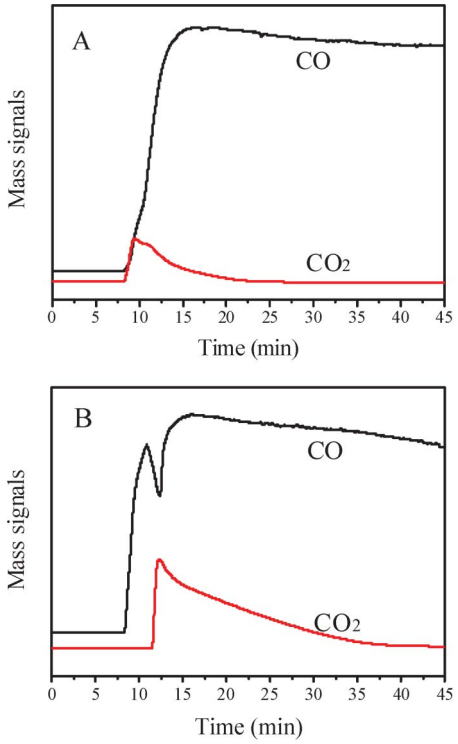

Fig. 9 The CO and CO_2 response curves obtained during the introduction of CO–He to Co_3O_4 (A) and $Fe_2Co_8O_x$ (B) at room temperature.

oxygen species from the bulk $Fe_2Co_8O_x$. This situation cannot be observed on Co_3O_4.

4. Discussion

The testing of the catalytic activities of the catalysts (Fig. 1) shows that adding iron to Co_3O_4 can obviously improve its catalytic activity for CO oxidation and this can be attributed to the following reasons. (1) The addition of iron to Co_3O_4 gives the catalyst a higher BET surface area. For instance, the BET surface area (109 $m^2\ g^{-1}$) of the $Fe_2Co_8O_x$ sample (Fe : Co = 2 : 8 (mol)) is much larger than that (~60 $m^2\ g^{-1}$) of Co_3O_4 or Fe_2O_3, and no agglomeration of this crystallite sample can be observed (Fig. 3b). Moreover, the Fe_2O_3 peaks cannot be observed in the XRD profiles (Fig. 2) and Raman spectra (Fig. 4). The iron ions have been incorporated into the spinel structure of Co_3O_4, forming the ferrite-like species in the $Fe_2Co_8O_x$ catalyst. (2) The XPS results indicate that the ratio of Co^{3+} : Co^{2+} on the $Fe_2Co_8O_x$ surface is higher than that on Co_3O_4 (Fig. 5). As Co^{3+} is the active site, a surface enriched with Co^{3+} ions is beneficial for CO adsorption on the catalyst surface. (3) The H_2 reduction behaviour of Co_3O_4 is varied due to the presence of Fe (Fig. 6), and the reduction of Fe became easier due to the formation of a Fe–Co oxide solid solution in the $Fe_2Co_8O_x$ sample. $Fe_2Co_8O_x$ possesses a better adsorption ability for CO than Co_3O_4 (Fig. 7). (4) The oxygen species on $Fe_2Co_8O_x$ are also more active than those on Co_3O_4, for

instance, $Fe_2Co_8O_x$ shows a very strong desorption of oxygen in its O_2-TPD curve (Fig. 8), and during the CO titration, its bulk lattice oxygen can more easily overflow to the surface to participate in the oxidation of CO (Fig. 9).

For the reaction mechanism of the CO oxidation, there are different viewpoints. Gamarra[47] and Sedmak[48] reported that the CO oxidation follows the Mars–van Krevelen mechanism. Others deem that it follows the Langmuir–Hinshelwood mechanism.[49] Li *et al.*[50] have proposed an Au-assisted Mars–van Krevelen mechanism for the CO oxidation on Au–FeO_x, where the support supplies surface lattice oxygen to react with CO adsorbed on the neighboring gold nanostructures which produces CO_2 and is accompanied by the reduction of Fe^{3+} to Fe^{2+}. The time-resolved CO titration in Fig. 9, obtained after the catalyst was pretreated at 600 °C in flowing He to remove the oxygen desorption species, shows that the CO_2 peak on $Fe_2Co_8O_x$ is more intense and broad than that on Co_3O_4, indicating that the bulk lattice oxygen in $Fe_2Co_8O_x$ more actively diffuses to the surface to fill the oxygen vacancies and takes part in the CO oxidation. The low-temperature oxygen desorption peak is pretty small when compared with the lattice oxygen on the Co_3O_4 sample, and its lattice oxygen became more active by adding iron (Fig. 8).

We propose that $Fe_2Co_8O_x$ catalyses the CO oxidation by the Mars–van Krevelen mechanism. The CO adsorbed on the catalyst surface reacts with surface oxygen to form CO_2, and the produced CO_2 desorbs from the surface to form an oxygen vacancy, which is filled by lattice oxygen or gas phase oxygen, and this builds a reduction–oxidation cycle. The results above show that the lattice oxygen of $Fe_2Co_8O_x$ is much more active than that of Co_3O_4, and it can oxidise CO at room temperature even without gas phase oxygen for a longer time than when using the Co_3O_4 catalyst. This is because Co_3O_4 contains less active lattice oxygen than $Fe_2Co_8O_x$. Therefore, it has been shown that adding iron to the Co_3O_4 catalyst improves the reactivity of the bulk lattice oxygen and the adsorption property for CO, which accelerates the reduction–oxidation cycle and increases its catalytic performance for CO oxidation.

Another important fact is that the addition of iron enhances the ratio of Co^{3+} : Co^{2+} on the surface, which is corroborated by the XPS result (Fig. 5), and when Co : Fe = 8 : 2 in the $Fe_aCo_bO_x$ sample the appropriate ratio of Co^{3+} : Co^{2+} on the catalyst surface can be obtained. Co^{3+} ions are the active sites for catalysing CO oxidation.[33,35] This is an essential reason for the iron modified Co_3O_4 catalyst having a higher activity for CO oxidation.

Furthermore, after He pretreatment at 600 °C, a cleaner surface can be obtained on the iron modified catalysts by removing most of the surface hydroxyl groups, which is also very important to initiate CO oxidation on the surface, and is further evidence that the CO oxidation over the $Fe_2Co_8O_x$ catalyst follows the Mars–van Krevelen mechanism.

5. Conclusion

In summary, iron modified Co_3O_4 ($Fe_aCo_bO_x$) catalysts for CO oxidation have been developed. The results show that the presence of iron increases obviously the catalytic activity of the Co_3O_4 catalyst for CO oxidation, and the appropriate ratio of Co : Fe is 8 : 2 (that is $Fe_2Co_8O_x$). Using this $Fe_aCo_bO_x$ catalyst, CO can be completely converted to CO_2 at −80 °C. The promotional role of Fe in the $Fe_aCo_bO_x$ catalyst may be attributed to the following reasons:

(1) the iron ions are incorporated into the spinel structure of Co_3O_4, resulting in an increase in the surface area of the catalyst and an inhibition of the agglomeration of iron oxide;

(2) the presence of Fe improves the reduction behaviour of Co_3O_4 and optimizes the ratio of Co^{3+} : Co^{2+} on the catalyst surface through interactions between the Fe and Co components, and promotes CO adsorption and CO_2 desorption on the catalyst surface;

(3) the oxygen species on $Fe_aCo_bO_x$ are more active than those on Co_3O_4, and when the feed gas is lacking in oxygen the lattice oxygen of $Fe_aCo_bO_x$ can easily overflow to the surface to participate in the oxidation of CO.

The CO oxidation on the $Fe_aCo_bO_x$ catalyst follows a Mars–van Krevelen mechanism, in which the oxygen vacancies can be replenished by active lattice oxygen in $Fe_aCo_bO_x$.

Acknowledgements

This project was financially supported by the National Natural Science Foundation of China (21273150), the National Basic Research Program of China (2010CB732300, 2013CB933201), the national high technology research and development program of China (2012AA062703), the Fundamental Research Funds for the Central Universities, the ''ShuGuang'' Project (10GG23) and the Leading Academic Discipline Project (J51503) of Shanghai Municipal Education Commission and Shanghai Education Development Foundation.

Notes and references

1 T. Krichner, A. Donnerstag, A. Konig and Eigenberger, *Stud. Surf. Sci. Catal.*, 1998, **116**, 125.
2 G. Lenaers, *Sci. Total Environ.*, 1996, **189–190**, 139.
3 N. Lopez, T. V. W. Janssens, B. S. Clausen, Y. Xu, M. Mavrikakis, T. Bligaard and J. K. Nørskov, *J. Catal.*, 2004, **223**, 232.
4 Y. X. Shen, G. Z. Lu, Y. Guo and Y. Q. Wang, *Chem. Commun.*, 2010, **46**, 8433.
5 C. X. Xu, J. X. Su, X. H. Xu, P. P. Liu, H. J. Zhao, F. Tian and Y. Ding, *J. Am. Chem. Soc.*, 2007, **129**, 42.
6 M. F. Luo, Y. J. Zhong, X. X. Yuan and X. M. Zheng, *Appl. Catal., A*, 1997, **162**, 121.
7 S. H. Taylor, G. J. Hutchings and A. A. Mirzaei, *Chem. Commun.*, 1999, 1373.
8 C. M. Bae, J. B. Ko and D. H. Kim, *Catal. Commun.*, 2005, **6**, 507.
9 Y. Yu and F. Yung, *J. Catal.*, 1974, **33**, 108.

10 H. K. Lin, H. C. Chiu, H. C. Tsai, S. H. Chien and C. B. Wang, *Catal. Lett.*, 2003, **88**, 169.
11 J. Jansson, *J. Catal.*, 2000, **194**, 55.
12 J. Jansson, A. E. C. Palmqvist, E. Fridell, M. Skoglundh, L. Osterlund, P. Thormahlen and V. Langer, *J. Catal.*, 2002, **211**, 387.
13 X. W. Xie, Y. Li, Z. Q. Liu, M. Haruta and W. J. Shen, *Nature*, 2009, **458**, 746.
14 J. Li, G. Z. Lu, G. S. Wu, D. S. Mao, Y. Q. Wang and Y. Guo, *Catal. Sci. Technol.*, 2012, **2**, 1865.
15 N. M. Deraz, *Colloids Surf., A*, 2002, **207**, 197.
16 G. A. El-Shobaky and A. M. Ghozza, *Mater. Lett.*, 2004, **58**, 699.
17 L. Daza, C. M. Rangel, J. Baranda, M. T. Casais, M. J. Martinez and J. A. Alonso, *J. Power Sources*, 2000, **86**, 329.
18 H. H. Kung, *Transition Metal Oxides: Surface Chemistry and Catalysis*, Elsevier, Amsterdam, 1989.
19 C. K. Rofer-DePoorter, *Chem. Rev.*, 1981, **81**, 447.
20 M. Haruta, N. Yamada, T. Kobayashi and S. Iijima, *J. Catal.*, 1989, **115**, 301.
21 L. Q. Liu, F. Zhou, L. G. Wang, X. J. Qi, F. Shi and Y. Q. Deng, *J. Catal.*, 2010, **274**, 1.
22 M. M. Natile and A. Glisenti, *J. Mol. Catal. A: Chem.*, 2004, **217**, 175.
23 T. C. Xiao, S. J. Ji, H. T. Wang, K. S. Coleman and M. L. Green, *J. Mol. Catal. A: Chem.*, 2001, **175**, 111.
24 Y. Brik, M. Kacimi, F. Bozon-Verduraz and M. Ziyad, *J. Catal.*, 2002, **211**, 470.
25 G. X. Wang, X. P. Shen, J. Horvat, B. Wang, H. Liu, D. Wexler and J. Yao, *J. Phys. Chem. C*, 2009, **113**, 4357.
26 J. Jiang and L. C. Li, *Mater. Lett.*, 2007, **61**, 4894.
27 D. Bersani, P. P. lottici and A. Montenero, *J. Raman Spectrosc.*, 1999, **30**, 355.
28 Q. Liu, L. C. Wang, M. Chen, Y. Cao, H. Y. He and K. N. Fan, *J. Catal.*, 2009, **263**, 104.
29 H. Y. Li, H. F. Wang, Y. L. Guo, G. Z. Lu and P. Hu, *Chem. Commun.*, 2011, **47**, 6105.
30 C. V. Schenck, J. G. Dillard and J. W. Murray, *J. Colloid Interface Sci.*, 1983, **95**, 398.
31 N. S. McIntyre and M. G. Cook, *Anal. Chem.*, 1975, **47**, 2208.
32 R. Riva, H. Miessner, R. Vitali and G. D. Piero, *Appl. Catal., A*, 2000, **196**, 111.
33 M. Kang, M. W. Song and C. H. Lee, *Appl. Catal., A*, 2003, **251**, 143.
34 Q. Guo and Y. Liu, *Appl. Catal., B*, 2008, **82**, 19.
35 E. Wilczkowska, K. Krawczyk, J. Petryk, J. W. Sobczak and Z. Kaszkur, *Appl. Catal., A*, 2010, **389**, 165.
36 M. Sorescu, R. A. Brand, D. Mihaila-Tarabasanu and L. Diamandescu, *J. Appl. Phys.*, 1999, **85**, 5546.
37 L. Xue, C. B. Zhang, H. He and Y. Teraoka, *Appl. Catal., B*, 2007, **75**, 167.
38 X. D. Hou, Y. Z. Wang and Y. X. Zhao, *Catal. Lett.*, 2008, **123**, 321.
39 Y. Y. Liu, T. Hanaoka, T. Miyazawa, K. Murata, K. Okabe and K. Sakanishi, *Fuel Process. Technol.*, 2009, **90**, 901.
40 D. Shanke, S. Vada, E. A. Blekkan, A. M. Hilmen, A. Hoff and A. Holmen, *J. Catal.*, 1995, **156**, 85.
41 G. Munteanu, L. Ilieva and D. Andreeva, *Thermochim. Acta*, 1997, **291**, 171.
42 O. J. Wimmers, P. Arnoldy and J. A. Moulijn, *J. Phys. Chem.*, 1986, **90**, 1331.
43 O. Lebedeva and W. H. M. Sachtler, *J. Catal.*, 2000, **191**, 364.
44 C. Li, K. Domen, K. Maruya and T. Onishi, *J. Chem. Soc., Chem. Commun.*, 1988, 1541.
45 Y. M. Choi, H. Abernathy, H. T. Chen, M. C. Lin and M. L. Liu, *ChemPhysChem*, 2006, **7**, 1957.
46 M. M. Schubert, S. Hackenberg, A. C. van Veen, M. Muhler, V. Plzak and R. J. Behm, *J. Catal.*, 2001, **197**, 113.
47 D. Gamarra, C. Belver, M. Fernández-García and A. Martínez-Arias, *J. Am. Chem. Soc.*, 2007, **129**, 12064.
48 G. Sedmak, S. Hocevar and J. Levec, *J. Catal.*, 2003, **213**, 135.
49 J. B. Wang, D. H. Tsai and T. J. Huang, *J. Catal.*, 2002, **208**, 370.
50 L. Li, A. Q. Wang, B. T. Qiao, J. Lin, Y. Q. Huang, X. D. Wang and T. Zhang, *J. Catal.*, 2013, **299**, 90.

